Nanoscale

PAPER

Check for updates

Tailoring defects in SrTiO₃ by one step nanoarchitectonics for realizing photocatalytic nitrogen fixation in pure water†

Ashish Kumar, [ID] [a,d] Manisha Sharma,‡[a] Sajjan Sheoran,‡[b] Shilpi Jaiswal,‡[c] Abhijit Patra, [ID] *[c] Saswata Bhattacharya [ID] *[b] and Venkata Krishnan [ID] *[a]

Surface contamination of materials by nitrogenous impurities is a major problem that can bias the quantification of ammonia in photocatalytic N₂ fixation reactions. In this work, SrTiO₃ nanocubes were prepared by using a nitrogenous precursor and engineered with Ti^{3+} sites and oxygen vacancy defects in a one-step solvothermal approach. It was observed that the synthesized materials were containing surface nitrogenous impurities and therefore a rigorous cleaning procedure was adopted to eliminate them to the best extent. The contribution of unavoidable surface impurities was deduced in the form of adventitious NH_3 by employing control experiments and a realistic photocatalytic NH_3 generation was achieved. It was found that pristine SrTiO₃ showed no photocatalytic activity, whereas one of the defected SrTiO₃ materials showed the highest NH_3 formation under natural sunlight in pure water, which was ascribed to the tuned defect sites, enhanced surface area and efficient separation of photogenerated charges. Based on the experimental results, a stringent protocol has been suggested for materials synthesis while working with nitrogenous precursors and for subsequent photocatalytic N₂ fixation experiments. Thus, the present study provides a simple and affordable procedure for catalyst synthesis for the studied application and expands the scope of perovskite oxide materials to fabricate efficient photocatalysts for sustainable NH_3 production.

[a]*School of Chemical Sciences and Advanced Materials Research Center, Indian Institute of Technology Mandi, Kamand, Mandi 175075, Himachal Pradesh, India. E-mail: vkn@iitmandi.ac.in*
[b]*Department of Physics, Indian Institute of Technology Delhi, New Delhi 110016, India. E-mail: saswata@physics.iitd.ac.in*
[c]*Department of Chemistry, Indian Institute of Science Education and Research Bhopal, Madhya Pradesh 462066, India. E-mail: abhijit@iiserb.ac.in*
[d]*Department of Chemistry, Sardar Patel University Mandi, Mandi 175001, Himachal Pradesh, India*
†Electronic supplementary information (ESI) available: Materials characterization, theoretical calculation details, XPS survey spectra, SEM images, TEM and HRTEM images, REELS spectra, BET study, XPS and EPR of recycled catalyst, elemental analysis, summary of photocatalytic NH_3 production, performance comparison table, modified indophenol method reactions, mass spectra and PL spectra. See DOI: https://doi.org/10.1039/d3nr01982a
‡These authors contributed equally to this work.

1 Introduction

Among different valuable chemicals produced on a large-scale worldwide, the contribution of ammonia (NH_3) is very high (235 million metric tons in 2019) and its production consumes about 1–2% of the global energy.[1,2] NH_3 is used as a main feedstock in different sectors, such as fertilizers for agriculture, pharmaceutical industries, synthetic fibers, dye indus-

tries, *etc.* and is also considered as a carrier for hydrogen gas due to its high hydrogen content.[3–6] In industries, NH_3 is manufactured by employing the Bosch-Haber process, which requires harsh conditions of temperature and pressure (15–30 MPa, 450 °C) and utilizes H_2 from the steam reforming process which releases a huge amount of CO_2 in the atmosphere.[7] It is likely that the demand for nitrogen-based fertilizers will continue to surge in the upcoming decades to cope with world hunger and hence the production of NH_3 will continue to increase for fulfilling different human requirements. This could cause an irreparable change in the environmental CO_2 levels and result in an energy crisis. Therefore, researchers are looking for alternate green approaches for the production of NH_3, since the current industrial process of NH_3 formation is not sustainable. In this regard, the conversion of sunlight into chemical energy is one of the fascinating routes to harvest renewable solar energy and photocatalytic nitrogen (N_2) fixation has emerged as a greener approach for the synthesis of this very important chemical.

Although the formation of NH_3 is thermodynamically feasible with $\Delta H = -92.2$ kJ mol^{-1}, the high bond dissociation energy of the triple bond of N_2 molecule makes this process difficult to carry out at ambient conditions.[8–10] Therefore, the

activation of N_2 molecules is the primary step for the success of this reaction over the surface of photocatalytic materials followed by the appropriateness of the position of band potentials, charge separation and transfer efficiency. The activation of N_2 molecules cannot occur on pristine surfaces and requires the engineering of necessary active sites. In this regard, several materials with oxygen vacancies have been reported for the photocatalytic N_2 fixation to NH_3.[7,11] It is noteworthy to mention that most of the materials reported for photocatalytic N_2 fixation utilize the chromogenic methods for the detection of NH_3 and use methanol as a sacrificial agent, which interferes in the quantification of NH_3. Therefore, it is highly desirable to develop such photocatalysts, which can work in pure water conditions. In such cases, chromogenic methods could be employed for the detection of NH_3 with more accuracy and reliability, if advanced instrumentation like ion chromatography and nuclear magnetic resonance are not available. In this regard, only a very limited number of materials with engineered defects have been known to exhibit photocatalytic N_2 fixation, such as F-doped TiO_2,[12] Cu-doped TiO_2,[13] InS_2,[14] Br doped $BiOCl$,[15] $BiOBr$,[16,17] Bi_5O_7Br[18] and g-C_3N_4.[19,20] Moreover, the bias in the quantification of photogenerated ammonia due to different factors like surface contamination of materials, gas purity, glassware contamination, *etc.* is generally not considered in many reports, which questions the reliability of reported data.[1,2] Therefore, it is very important to eliminate such factors by employing proper experimental protocols so that reproducible NH_3 production rates can be reported.

Alkaline earth-metal titanate-based perovskite oxides are also good options for oxygen vacancy engineering and exploration of the feasibility of photocatalytic N_2 fixation due to their highly negative conduction band potentials.[21–23] Particularly, $SrTiO_3$ is one of the most studied materials for different photocatalytic applications, such as pollutants degradation, CO_2 reduction and H_2 evolution owing to its high stability (thermal and chemical), outstanding photocorrosion resistance, ability to form different nanostructures and comparable band gap to the benchmark TiO_2.[1] $SrTiO_3$ is a wide band gap perovskite material, which can harvest UV region of the solar spectrum effectively.[24] To enhance its photoresponse and photocatalytic activity, several strategies like doping, composite formation and defect engineering have been employed.[25,26] Among these, defect engineering is a fascinating tool for altering the surface, optical and electronic properties of materials.[27] Previously, $SrTiO_3$ has been engineered with oxygen vacancies by annealing in the presence of $NaBH_4$ under Ar atmosphere,[28,29] annealing under H_2 atmosphere[30] and molten salt route,[31] and mainly utilized for photocatalytic H_2 evolution application. The defected $SrTiO_3$ reported for photocatalytic N_2 fixation has been prepared by hydrogenation of pristine sample and post-reduction using lithium alkylamine solution.[32,33] However, more simple synthesis routes need to be developed to cut down the cost of instrumental infrastructure and gases used in the above-mentioned synthesis procedures. In addition, it is highly important to determine the contribution

of nitrogenous impurities present on the surface of photocatalytic materials and eliminate their interference in the NH_3 quantification so that realistic NH_3 production rates should be reported.

Taking the above factors into consideration, we utilized a facile solvothermal method for the synthesis of defect-engineered $SrTiO_3$ photocatalysts and employed them for photocatalytic N_2 fixation in pure water and under natural sunlight irradiation. Here ascorbic acid was used as a reducing agent in varying amounts to tune the Ti^{3+} sites and oxygen vacancy in $SrTiO_3$ *via* one-step nanoarchitectonics.[34] X-ray photoelectron spectroscopy and electron paramagnetic spectroscopy were employed for the detailed investigation of defects in the obtained materials. For the detection of generated NH_3, Nessler's reagent method was employed along with the hydrazine detection method. The surface nitrogenous contaminations were monitored and removed to the best extent, and the contribution of impurities in the photogenerated NH_3 was deduced so that reliable NH_3 production rates can be achieved. $SrTiO_3$ with tuned defects exhibited the NH_3 formation in pure water during the photocatalytic reaction. Thus, the present study is anticipated to open a new area for exploring different perovskite oxide materials for defect engineering and photocatalytic N_2 fixation application.

2 Experimental section

2.1 Synthesis of $SrTiO_3$ (ST) and defect-engineered $SrTiO_3$ (DST)

The materials used for the synthesis of $SrTiO_3$ (ST) and defect-engineered $SrTiO_3$ (DST) were obtained from Sigma-Aldrich and were used without any modifications. The other materials used for the indophenol method (NaOH, salicylic acid, sodium hypochlorite and tri-sodium citrate) were obtained from Thermo-Fisher Scientific and Merck, India. The synthesis of pristine $SrTiO_3$ (white color) was carried out by employing an earlier reported procedure[35] with some optimizations. In a typical reaction, 1.46 mmol (0.43 mL) of titanium tetraisopropoxide (TTIP) was added to 60 mL of ethanol and kept stirring for about 15 min (solution 1). Secondly, 1.46 mmol (309.8 mg) $Sr(NO_3)_2$ was dissolved in 5 mL of deionized water to prepare solution 2. Subsequently, solution 2 was slowly added to solution 1 with constant stirring for about 30 min to obtain a turbid suspension. After 30 min of stirring, 6.8 g of NaOH was added to the above suspension and the mixture was allowed to stir for another 30 min to obtain a white suspension. This white suspension was transferred in a Teflon-lined stainless steel autoclave and kept in an oven at 160 °C for 24 h. For the synthesis of DST materials, a particular amount of ascorbic acid (1 g, 2 g and 3 g for DST1, DST2 and DST3, respectively) was directly added in the autoclave vessel before keeping in oven. It is noteworthy to mention that the addition of ascorbic acid in the white suspension resulted in the sticking of precipitates on the walls of the reaction flask. The final products were obtained from these reactions after cooling by

multiple ultrasonication and centrifugation washing of obtained solid by ethanol, dilute acetic acid, dilute HCl and deionized water. Dilute acetic acid and HCl were used to wash off the carbonates and nitrogenous impurities from these materials. Finally, the obtained solids were dried at 60 °C in an oven and ground to obtain the ST (white) and DST (pale brown to dark brown) powders with a yield of about 200 mg.

2.2 Photocatalytic N_2 fixation experiments

Photocatalytic N_2 fixation experiments were carried out under closed conditions in a 100 mL round bottom flask under natural sunlight irradiation ($9.5–10.2 \times 10^{-3}$ W cm^{-2}). In a typical reaction, 20 mg of photocatalyst was dispersed ultrasonically in 50 mL of ultrapure deionized water and the reaction vessel was evacuated with the help of a suction pump. Subsequently, highly pure N_2 gas was purged into the photocatalyst suspension at a rate of 100 mL min^{-1} for 1 h. Finally, the reaction was started by irradiating under natural sunlight and 1 mL samples were collected after each 30 min time interval with the help of a syringe. The collected samples were centrifuged at 12 000 rpm to remove the solid catalyst powder. For the quantification of generated NH_3, Nessler's reagent method was used.[36,37] After complete coloration (10–15 min), the concentration of NH_3 generated was estimated by monitoring and comparing the absorption at 420 nm against the absorption of standard NH_4Cl aqueous solutions. In addition, the detection of hydrazine was also performed by employing a previously reported procedure.[38]

To ensure that the NH_3 has been formed from the purged N_2 gas, the photocatalytic experiments with isotope-labeled $^{15}N_2$ gas were performed under similar conditions. The Indophenol method was used for the detection of the formed products. In this method, NH_4^+ ions react with salicylic acid and sodium hypochlorite to form a colored compound called indophenol.[39,40] First, 1 mL of suspension was taken out from the reaction mixture and was centrifuged to remove the catalyst. Then, 1 mL of 1 M NaOH containing 0.5 M salicylic acid and 0.2 M sodium citrate was added followed by 50 μL addition of sodium hypochlorite. After that, 0.2 mL of 1 wt% aqueous solution of sodium nitroferricyanide was added. The solutions were mixed and left for 1 h to develop the color and subjected to mass spectroscopy analysis.

3 Results and discussion

The synthesis of ST and DST materials was carried out by employing a one-step solvothermal method, wherein a varying amount of ascorbic acid was used as a reducing agent to engineer the defects in resulting samples. The salient features of the synthetic procedure are presented in Scheme 1.

Initially, powder X-ray diffraction (PXRD) measurements were performed to inveterate the successful formation of as-synthesized materials and obtained results are presented in Fig. 1a. The PXRD peaks for ST can be assigned to the cubic phase of $SrTiO_3$ and confirms its high phase purity (JCPDS no. 35-0734).[35] For DST materials prepared by using different amounts of ascorbic acid, the PXRD patterns were quite similar to that of pristine ST. However, the color of DST materials was different ranging from pale to dark brown, which indicates the surface alterations. Since Raman spectroscopy is a more sensitive technique for the study of crystal structure and surface defects, therefore, Raman spectroscopic investigations were performed to investigate the surface modi-
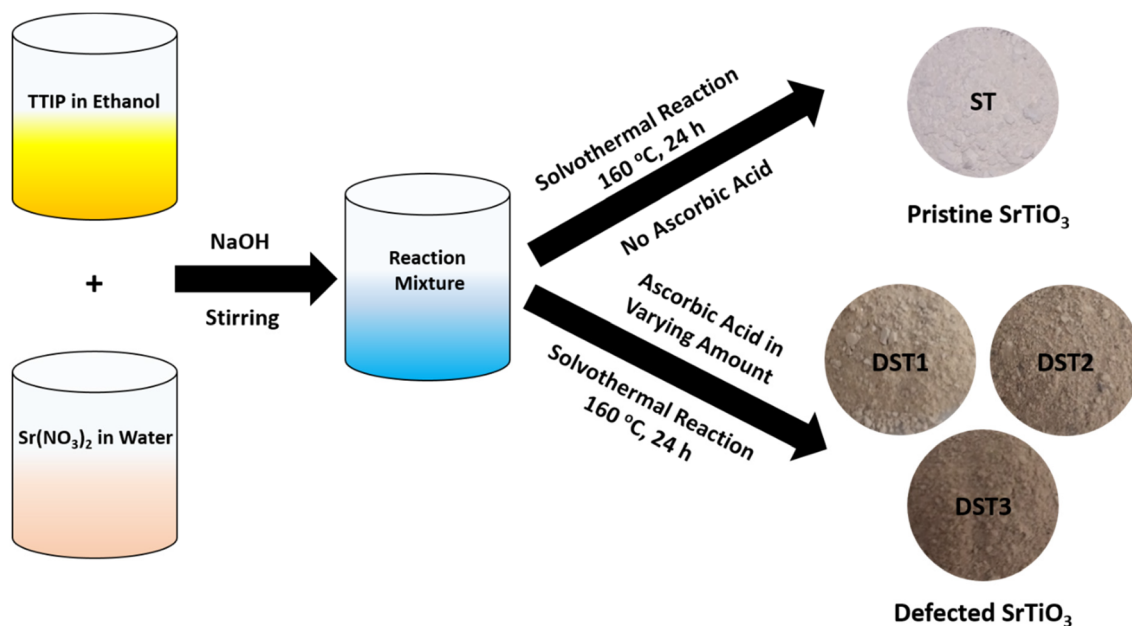
Scheme 1 Schematic presentation of synthesis of pristine ST (synthesized without using ascorbic acid) and defect-engineered DST materials (synthesized by using varying amounts of ascorbic acid).
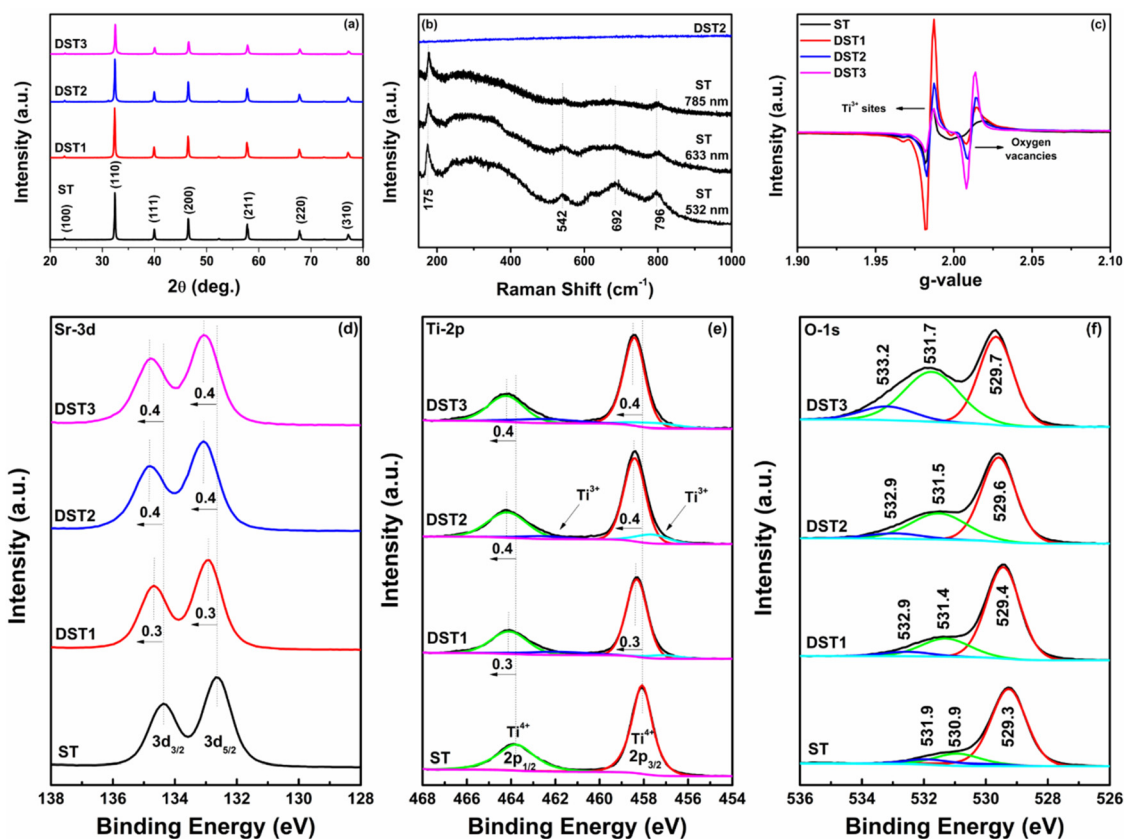
Fig. 1 (a) PXRD patterns, (b) Raman spectra, (c) EPR spectra and high-resolution X-ray photoelectron spectroscopy (d) Sr-3d, (e) Ti-2p and (f) O-1s spectra of ST and DST materials.

fications. For this study, three different lasers (532 nm, 633 nm and 785 nm) were used at different values of power and gratings. The pristine ST showed well-defined peaks at 175 cm⁻¹, 542 cm⁻¹, 692 cm⁻¹ and 796 cm⁻¹ with all three lasers, which can be assigned to the cubic crystal structure of $SrTiO_3$.[41] However, the Raman spectra of DST2 material was remained flattened in comparison to the pristine ST with all lasers used at different powers and gratings. This type of behavior has already been reported by defect-rich materials and is the signature of crystal structure disorders and more heterogeneous surfaces in such materials.[41–43] Thus, it can be concluded that the use of ascorbic acid in the solvothermal reaction results in the formation of surface defects in DST materials. The change in color from white for pristine ST to brownish for DST materials signifies the introduction of defects in DST materials.

Furthermore, to study the nature of defects introduced in ST by using ascorbic acid, electron paramagnetic resonance (EPR) spectroscopic analysis was performed and corresponding results are presented in Fig. 1c. The g-values for ST, DST1, DST2 and DST3 are calculated as 1.98 and 2.01, which were attributed to Ti^{3+} sites (paramagnetic, 3d¹) and oxygen vacancy, respectively.[31,44,45] It was observed that the pristine ST sample also contained some fractions of Ti^{3+} sites and oxygen vacancy due to intrinsic non-stoichiometry, resulting in the

EPR signals.[44] For DST materials, the peak intensity at g = 2.01 increased from sample DST1 to DST3, which signifies an increase in oxygen vacancies. However, the peak intensity at g = 1.98 decreased from sample DST1 to DST3, suggesting a decrease in Ti^{3+} sites. This could be due to the localization of electrons trapped in the oxygen vacancies, which inhibit their transfer to adjacent Ti^{4+} sites and hinder the formation of Ti^{3+} sites.[46,47] Moreover, a decreased concentration of Ti^{3+} sites has been reported as beneficial for photocatalytic applications.[33,48,49]

In addition, a detailed X-ray photoelectron spectroscopy (XPS) analysis was also performed to study the defects and the corresponding results are presented in Fig. 1d–f. The survey spectra for all materials are provided in Fig. S1 in the ESI,† which confirms the high purity and presence of Sr, Ti and O constituents. In addition, high-resolution C-1s spectra have been provided in Fig. S2,† which are showing similar adventitious carbon peaks in all the samples.[50] It can be seen from Fig. 1d that the high-resolution Sr-3d spectra of pristine ST showed two distinct peaks at 132.7 eV ($3d_{5/2}$) and 134.4 eV ($3d_{3/2}$).[51] However, for DST materials prepared by varying amounts of ascorbic acid, these peaks were shifted towards higher binding energy. In the Sr-3d spectra of DST1, a positive and symmetric shift of 0.3 eV was observed in both these peaks, which was increased to 0.4 eV for DST2 and DST3. In

Ti-2p spectra of pristine ST, the two symmetric peaks at 458.1 eV ($2p_{3/2}$) and 463.8 eV ($2p_{5/2}$) were observed, which confirm the +4 oxidation state of Ti in $SrTiO_3$ (Fig. 1e).[51,52] Similar to the Sr-3d spectra of DST1, DST2 and DST3 materials, a symmetric shift of 0.3 eV and 0.4 eV was observed in the Ti-2p spectra of these materials. This type of positive symmetric shift has been known to arise from the characteristic shift of the Fermi level and can be ascribed to the oxygen vacancies introduced in the materials.[31] In addition, the high-resolution XPS spectra of DST materials provided another important evidence for the formation of Ti^{3+} sites on their surface.[41] Furthermore, we performed the surface etching to reveal the presence of Ti^{3+} sites in the bulk of the DST2 material (Fig. S3†). It was found that the concentration of Ti^{3+} sites was not diminished even after 200 seconds of surface etching, which confirm the existence of Ti^{3+} sites in the subsurface and bulk of the DST2 material.

Furthermore, the XPS O-1s spectra of pristine ST showed three deconvoluted peaks at 529.3 eV, 530.9 eV and 531.9 eV, which arise from the oxygen present in the crystal structure, surface hydroxyl groups and oxygen vacancies, respectively (Fig. 1f).[28,53,54] This confirms that there were some oxygen vacancies present in pristine ST also, which is also consistent with the EPR data. In the case of DST1, the O-1s spectra showed a slight shift of crystal structure oxygen peak (529.4 eV) towards higher binding energy. There were two new peaks evidenced in DST1 O-1s spectra at 531.4 eV and 532.9 eV, which can be assigned to the oxygen molecules adsorbed on oxygen vacancies and water molecules present on the catalyst surface.[51] For DST2 and DST3, these peaks were further shifted toward higher binding energy as shown in Fig. 1f. In addition, the peak intensity of oxygen molecules chemically adsorbed on oxygen vacancies follows the order: DST1 < DST2 < DST3. This indicates that the amount of oxygen vacancies got increased in these samples with an increase in the amount of ascorbic acid used in the solvothermal reaction and follows the following trend: DST3 > DST2 > DST1. Therefore, from XPS results, it can be concluded that the Ti^{3+} sites and oxygen vacancies were introduced onto the surface, subsurface and bulk of the DST materials, which is consistent with the observation of defects from Raman and EPR analysis.

The morphology of pristine ST and representative DST2 materials was investigated by scanning electron microscopy (SEM) and corresponding images are presented in Fig. S4.† It can be seen from Fig. S4a and b† that pristine ST possesses cube-like morphology along with very few hollow nanocubes. The nanocubes of different sizes were formed predominantly in ST in the absence of ascorbic acid in the reaction mixture. On the other hand, in DST2 material, the hollow nanocubes can easily be seen along with the porous aggregates, in addition to the well-defined nanocubes (Fig. S4c and d†). From this study, it can be concluded that the ascorbic acid used in the synthesis of DST materials has resulted in morphological changes. This could be due to the inhibition of hydrolysis of Sr^{2+} ions during the reaction which limits the growth of the $SrTiO_3$ crystals and results in the morphological deformations.[55,56] Furthermore, transmission electron microscopy (TEM) and high-resolution TEM (HRTEM) measurements were performed to study the morphology and disorders in ST and DST2 more deeply. It can be seen from Fig. 2a and b that pristine ST showed the nanocube-like morphology with different sizes. In HRTEM analysis of pristine ST (Fig. 2c), uniform lattice fringes with 0.271 nm spacing corresponding to (110) plane were observed. Subsequently, the fast Fourier transform (FFT) image shown in Fig. 2d was collected from the selected area of Fig. 2c (in the yellow box) and inverse FFT (IFFT) was processed for the same as shown in Fig. 2e. It was found that the lattice fringes in pristine ST were uniform and well-ordered, which suggests that this sample was mostly free from defects. For DST2, it was observed that the solid cube-like morphology was not retained completely and some porous aggregates and hollow cubes were also formed (Fig. 2f and g). In addition, the disrupted lattice fringes were captured in DST2 along with the uniform fringes, which signifies the formation of defects in this material due to the use of ascorbic acid in the synthesis process. Fig. 2h shows that lattice fringes were disrupted in region (i) and were uniform in region (ii) with 0.271 nm spacing.

To investigate both of these regions, FFT and IFFT were processed (Fig. 2i and j) from the selected area of Fig. 2h and the deformation of lattice fringes was confirmed. In addition, the line-scan analysis of these regions was also performed (Fig. 2k), which confirmed the disturbance in the width of lattice fringes due to the presence of defects in DST2. Additional HRTEM images have been provided for ST and DST2 in Fig. S5† to display similar observations. Also, the porous aggregates were found to be crystalline in nature as shown in Fig. S6.† Furthermore, energy dispersive X-ray analysis (EDAX) and elemental mapping were also performed for DST2 material to analyze the composition. The EDAX data of DST2 is provided in Fig. 2l, which confirms the presence of its constituent elements. Fig. 2m shows the scanning TEM image of DST2 material along with the selected area (in the yellow box) for elemental mapping. The elemental overlay and individual elemental mapping are shown in Fig. 2n–q, which confirms the distribution of constituent elements in the selected area. Overall, these studies confirmed the successful formation of defects in DST2, as evidenced by Raman, EPR and XPS studies.

Subsequently, the optical properties of as-synthesized materials have been studied by employing diffuse reflectance spectroscopy (DRS) and the obtained absorption plots along with the band gap values obtained from Tauc plots are presented in Fig. 3a and b.[57] Pristine ST showed the absorbance in UV region, which corresponds to a band gap of 3.21 eV in agreement with literature reports.[58] With the introduction of ascorbic acid in the solvothermal reaction, the resulting DST materials started absorbing also in the visible light region of the solar spectrum. It can be seen that for DST1, there was a slight decrease in the band gap from 3.21 eV to 3.16 eV, with a tail-like absorption in the visible light. For DST2, the band gap was drastically decreased to 2.99 eV due to further enhance-
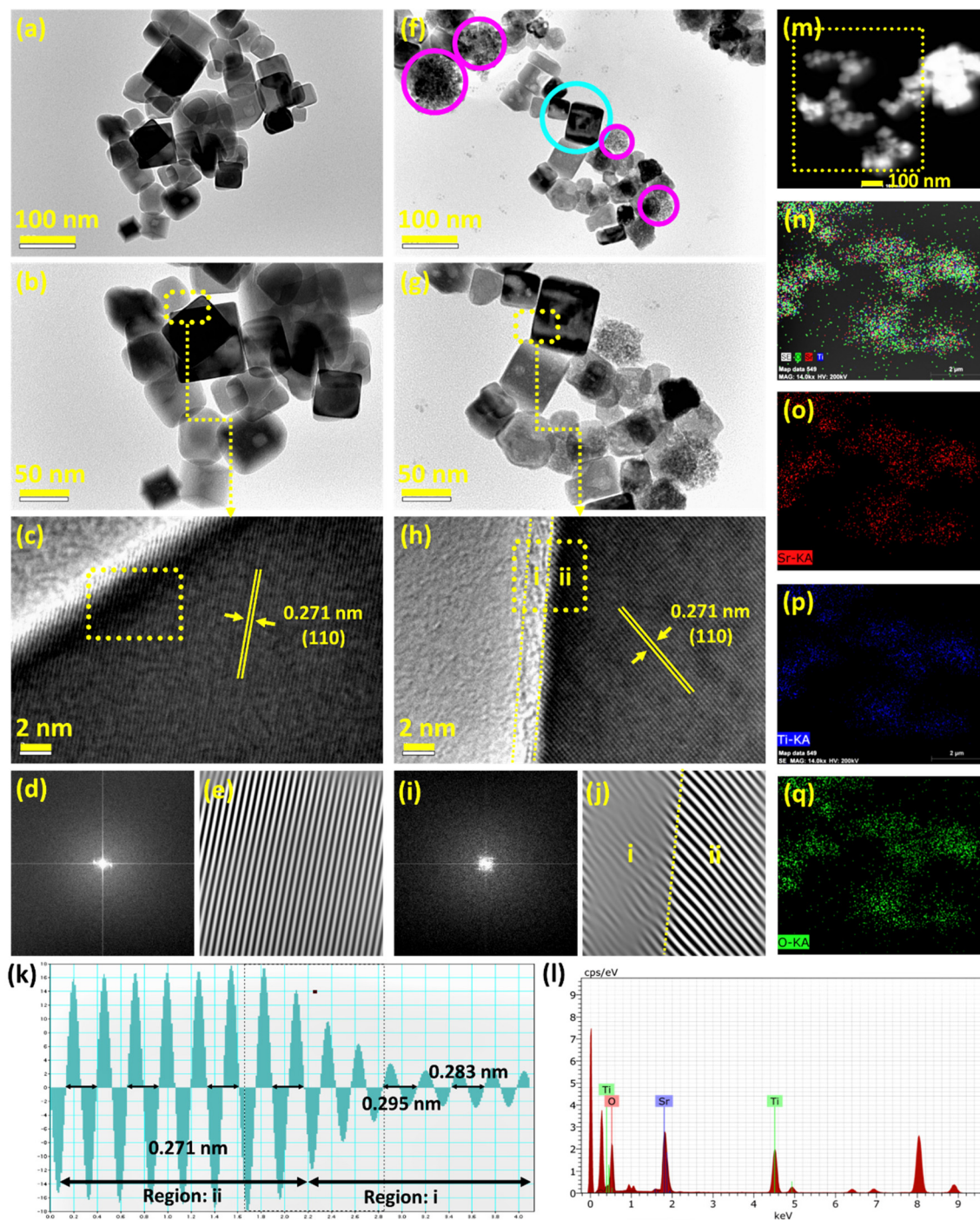
Fig. 2 (a, b) TEM images, (c) HRTEM image of ST and (d, e) FFT and IFFT of the selected region of image (c) showing the uniform lattice fringes; (f, g) TEM images of DST2 with morphological variations (hollow nanocubes encircled cyan and small aggregates encircled pink), (h) HRTEM image of DST2 showing the disrupted region (i) and uniform region ii of lattice fringes and (i–k) FFT, IFFT and line profile of the selected region of image (h) showing the uniform and disrupted lattice fringes in respective regions; (l) EDAX spectra and (m–q) elemental mapping of DST2.

ment in ascorbic acid amount and a more prominent visible light absorption was observed. A subsequent increase in the ascorbic acid resulted in a further decrease in the band gap to 2.85 eV in DST3 with the most prominent visible light absorption band. The band gap values of ST and DST2 were also confirmed by reflected electron energy loss spectroscopy (REELS) and found to be 3.20 eV and 3.01 eV, respectively, which are consistent with those obtained from Tauc plots (Fig. S7†). The change in the color of pristine ST from white to brownish in DST samples indicates the introduction of
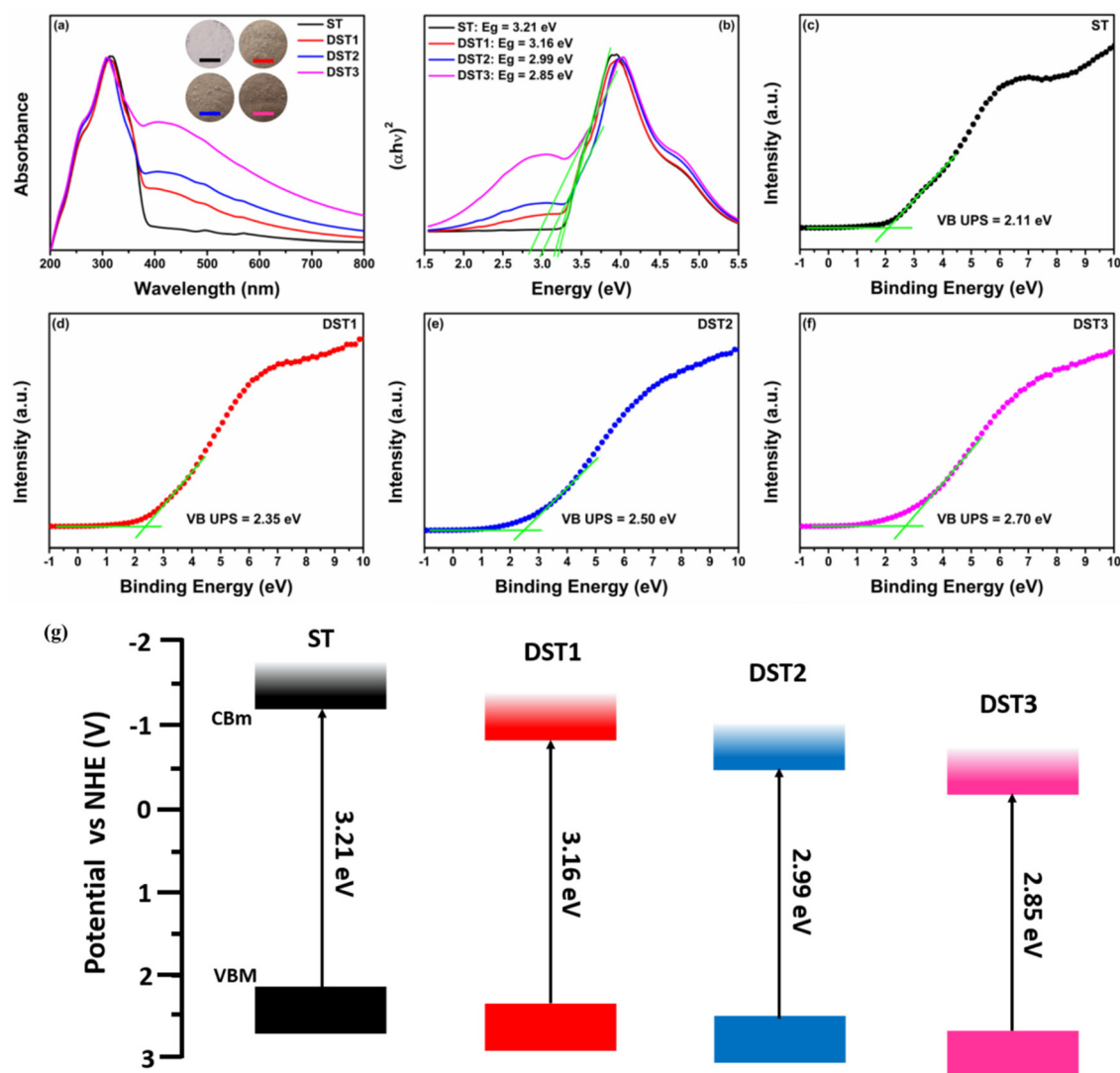
Fig. 3 (a) Diffuse reflectance spectroscopy absorption spectra (inset: photographs of samples), (b) Tauc plots for band gap calculations, (c–f) ultra-violet photoelectron spectroscopy VB spectra and (g) band diagram of pristine ST and defected DST materials.

defects in them, which is consistent with other reported materials.[13,59] Thus, it can be concluded that the formation of defects during the solvothermal synthesis of DST materials resulted in enhanced light absorption in the visible region of solar spectrum. Furthermore, ultraviolet photoelectron spectroscopy (UPS) was employed to study the position of valence band maxima (VBM) in these materials (Fig. 3c–f). The VBM for pristine ST was observed at 2.11 eV. For DST materials, the VBM position was shifted downwards with an increase in the ascorbic acid amount used in their synthesis. The VBM values were lowered to 2.35 eV, 2.50 eV and 2.70 eV for DST1, DST2 and DST3, respectively. By utilizing the VBM positions and band gap values, the conduction band minimum (CBm) values were calculated and found to be −1.10 eV, −0.81 eV, −0.49 eV and −0.15 eV for ST, DST1, DST2 and DST3. The band diagram obtained from these investigations is depicted in Fig. 3g.

In addition, BET measurements were also performed to study the change in specific surface area with the use of ascorbic acid in the solvothermal reaction. The adsorption–desorption isotherms and BET surface area plots are presented in Fig. S8.† It is likely that the morphological changes observed in SEM study indicate the change in specific surface area of DST materials in comparison to the pristine ST. It can be seen that pristine ST showed a specific surface area of 21.1 m^2 g^{-1}. For DST1, a slight increase in the specific surface area was observed (24.2 m^2 g^{-1}), whereas DST2 showed more enhanced specific surface area (32.7 m^2 g^{-1}) in comparison to the pristine ST. This increase in the surface area can be attributed to the increase in the amount of ascorbic acid used during the solvothermal reaction. For DST3, the surface area was further enhanced to 43.6 m^2 g^{-1} with an increase in the ascorbic acid amount used during synthesis. Thus, it can be concluded that defect-engineered DST samples showed higher

specific surface area in comparison to the pristine ST and this increase is directly proportional to the amount of ascorbic acid used during their synthesis.

The study of photocatalytic performance of pristine ST and DST materials was carried out by comparing their N_2 fixation capabilities. The photocatalytic N_2 fixation experiments were performed in pure deionized water without using any sacrificial agent and in the presence of natural sunlight irradiation. Before performing the photocatalytic N_2 fixation experiments, it was ensured that the surface of as-synthesized materials is free from nitrogenous impurities to the best extent, which is necessary to ensure the correctness of the obtained results as reported by Zhang and coworkers.[60] For this, the catalysts were carefully washed by using ultrasonication and centrifugation under different solutions and solvents as explained in the synthesis procedure. To confirm the removal of surface nitrogenous impurities, the surface elemental composition was determined from the XPS data and it was found that a small amount of nitrogen was present in DST samples even after rigorous washing (Table S1†). Firstly, the overall time-dependent generation of NH_3 in the N_2 atmosphere was obtained by using Nessler's reagent quantification method, under pure

water medium and obtained results are presented in Fig. 4a. To deduce the contribution of nitrogenous impurities in the obtained NH_3 production rate, the control photocatalytic experiments were performed under Ar atmosphere (in the absence of N_2 gas) (Fig. 4b). In addition, both Ar and N_2 gases purged in pure water did not show the presence of adventitious NH_3 in them. It can be seen from Fig. 4b that ST and DST1 catalysts did not show any NH_3 formation under Ar atmosphere. On the other hand, DST2 and DST3 catalysts showed a small amount of NH_3 formation (8.11 μmol h^{-1} and 7.59 μmol h^{-1}, respectively), which can be ascribed to the contribution from the photocatalytic reduction of nitrogenous impurities. In Fig. 4c, the realistic amount of NH_3 is presented after subtracting the contributions due to nitrogenous impurities. For pristine ST, it was observed that there was no formation of NH_3 after 120 min of sunlight irradiation. This inactivity of pristine ST could be ascribed to the absence of sufficient active sites on its surface, which helps in the chemisorption of N_2 molecules and subsequent reduction under light irradiation. However, for defect-engineered DST materials, the formation of NH_3 was observed in pure water. The DST1 material prepared by using the lowest amount of
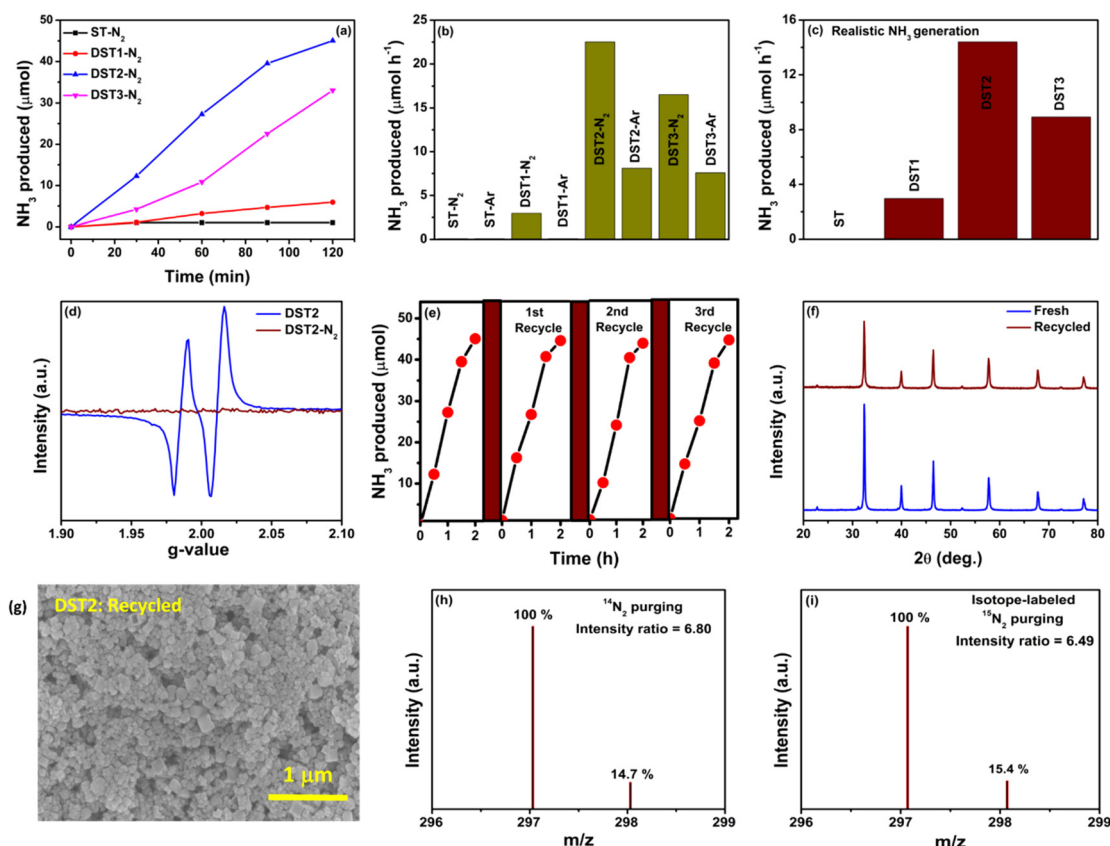

Fig. 4 (a) Time-dependent NH_3 production under N_2 atmosphere, (b) NH_3 produced per hour under N_2 atmosphere and Ar atmosphere control experiments, (c) realistic rate of NH_3 production obtained after subtracting the nitrogenous impurities contribution (photocatalyst amount 20 mg in 50 mL deionized water), (d) EPR spectra of DST2 in water before and after N_2 purging, (e) recyclability of DST2 for three cycles, (f) comparison of PXRD patterns of fresh and recycled DST2, (g) SEM image of recycled DST2 catalyst and mass spectra obtained for (h) $^{14}N_2$ gas and (i) isotope-labeled $^{15}N_2$ gas purged reaction samples.

ascorbic acid showed a slight improvement in the photocatalytic N_2 fixation and showed the generation of about 2.96 μmol h^{-1} NH_3. For DST2 prepared by using a moderate amount of ascorbic acid, the N_2 fixation was significantly enhanced as NH_3 was generated at a rate of 14.41 μmol h^{-1}. For DST3 prepared by using the highest amount of ascorbic acid, the photocatalytic N_2 fixation ability was lower than DST2, wherein NH_3 was generated at a rate of 8.93 μmol h^{-1}. A detailed summary of photocatalytic N_2 fixation results is provided in Table S2.†

The photocatalytic performance of DST2 was the best among all the prepared materials and could be ascribed to the appropriate amount of defects or surface active sites introduced in it, which corroborates well with the light absorption and photogenerated charge separation properties, in addition to providing the abundant reaction sites for chemisorption of N_2 molecules. On the other hand, the decrease in the activity of DST3 can be attributed to the excess amount of defects present in DST3, which results in the higher recombination of photogenerated charges in comparison to DST2. Another important factor that controls the photocatalytic performance of semiconductor photocatalysts is surface area. Although the surface area of DST3 was found to be higher than DST2, the decline in the photocatalytic performance of DST3 suggests the dominance of photogenerated charge recombination in it. To confirm the role of defect sites in the adsorption of N_2 molecules, EPR measurements were performed by dispersing the DST2 material in deionized water before and after N_2 purging (Fig. 4d). It was found that the EPR signals of oxygen vacancies and Ti^{3+} sites vanished upon purging of N_2 gas in the DST2 dispersion. This confirms that the engineered defect sites contribute to the adsorption of N_2 gas molecules on the catalyst surface.

The recyclability and stability of a photocatalyst are other important parameters in addition to the photocatalytic performance evaluation. Herein, the recyclability of DST2 was checked for 3 cycles, wherein the sample collection for NH_3 quantification was done on 3 different sunny days. It can be seen from Fig. 4e that the overall amount of NH_3 generated was not significantly changed during this study, which suggests the excellent recyclability of DST2 catalyst for this reaction. The sample recovered after the recyclability study was subjected to structural and morphological stability analysis. The comparison of PXRD patterns and SEM images of fresh and recovered catalysts confirms the good structural and morphological stability of DST2 (Fig. 4f and g). To study the stability of defects, EPR and XPS measurements were performed on recycled DST2 catalyst and the obtained spectra were compared with fresh DST2. In O-1s XPS spectra of recycled DST2 (Fig. S9†), the characteristic peak of oxygen vacancies was observed at 531.9 eV, which appeared at 531.5 eV in fresh DST2 due to the adsorption of O_2 molecules on vacancy sites. This infers desorption of adsorbed O_2 molecules during the photocatalytic reaction. On the other hand, the comparison of EPR spectra showed a slight decrease in the intensity for recycled DST2 (Fig. S10†), which can be ascribed to the very

minor loss of defects during the repetitive reaction cycles. However, both of these studies revealed the appreciable stability of defects after recyclability with negligible loss in photocatalytic performance. In addition, the comparison of the photocatalytic performance of DST2 with other defect-engineered materials is provided in Table S3,† which reveals that its N_2 fixation ability is comparable to the other reported materials.

To verify the source of nitrogen in generated NH_3, the photocatalytic experiments were performed under isotope-labeled $^{15}N_2$ gas atmosphere and a modified indophenol method followed by mass spectroscopy was employed for product analysis. The reactions involved and products identified by mass spectroscopy are presented in Fig. S11.† In addition, the control experiments with pure water, standard ammonia and $^{14}N_2$ gas atmosphere were also performed and the obtained mass spectra are presented in Fig. S12.† In the case of pure water, no peaks were observed in the expected mass spectral region, which confirms the absence of NH_3 as an impurity in it. For a standard NH_3 solution, the peaks around $m/z = 297$ and 298 were observed with an intensity ratio (I_{297}/I_{298}) of 6.89. For the sample collected from the reaction mixture purged with $^{14}N_2$ gas, similar peaks were observed with an intensity ratio of 6.80, which is comparable with that obtained for standard NH_3 solution (Fig. 4h). With isotope-labeled $^{15}N_2$ gas, an increase in the peak intensity at $m/z = 298$ was expected with the formation of $^{15}NH_3$ and the same could be evidenced experimentally. Due to this reason, it can be observed from Fig. 4i that the intensity ratio was significantly decreased to 6.49. This confirms the generation of NH_3 from the purged nitrogen gas.

Furthermore, density functional theory (DFT) calculations are performed to theoretically investigate the role of defects in the photocatalytic N_2 fixation process (for computational details, see ESI†). The cubic structure of ST having space group $Pm\bar{3}m$ is shown in Fig. 5a. Fig. 5b and c show the partial density of states (pDOS) for pristine and defected ST, respectively. In pristine ST, the VBM mainly consists of O-2p orbitals and Ti-3d orbitals contribute to the CBm with a wide band gap of 3.21 eV (Fig. 5b) and are found to be consistent with the experimental observation. The states are symmetric concerning the spin orientation in pristine ST due to the absence of any unpaired electron. The Fermi level lies just above the VBM, which makes pristine ST a p-type material. In defected ST, the defect states are localized near the CBm and the Fermi level gets shifted just below the CBm (Fig. 5c). Since the defect states are near the CBm, it excludes the chances of these states acting as recombination centers. The defect states are asymmetric due to the presence of unpaired electrons. Therefore, these states act as donor states and the defected system becomes stable after releasing the two electrons. Therefore, the defected system helps in the reduction of N_2 by providing extra electrons to produce NH_3. In addition, the alignment of the band edges of pristine and defected ST was performed to check the suitability of band edges for photocatalytic N_2 fixation. For the reduction of N_2, the CBm should lie above the
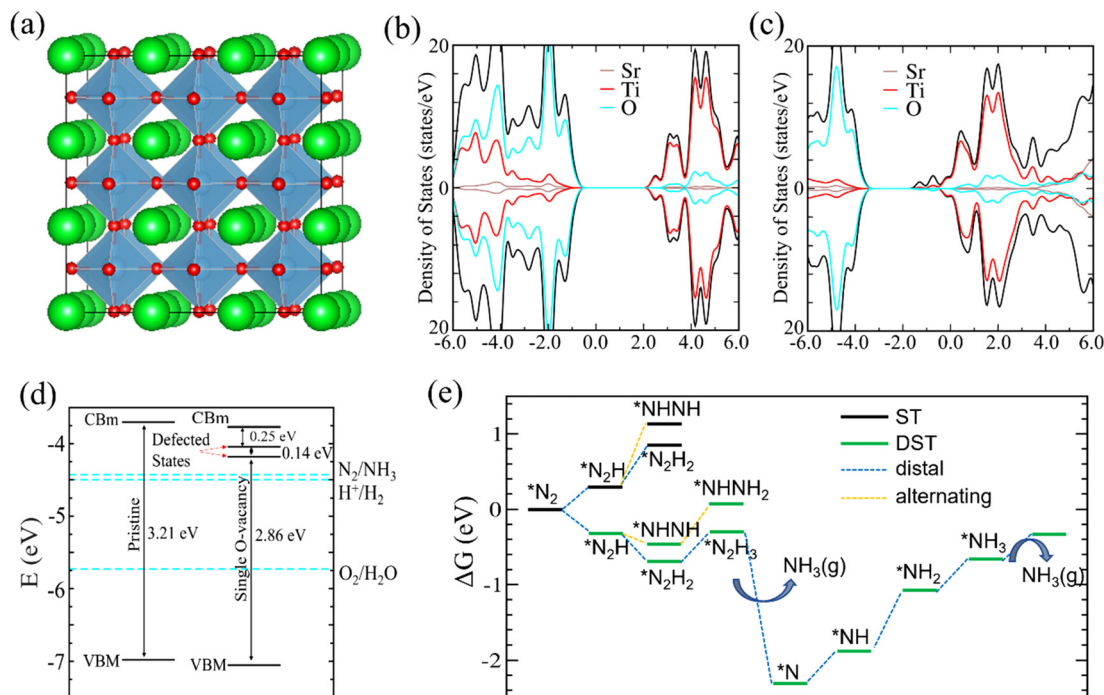
Fig. 5 (a) The 3 × 3 × 3 supercell of ST with cubic $Pm\bar{3}m$ space group symmetry (green, cyan and red colors show Sr, Ti and O atoms, respectively). The TiO$_6$ octahedra are shown in light cyan color. Partial density of states (pDOS) of (b) pristine and (c) defected ST. (d) Band edge alignment of pristine and defected ST. (e) Calculated Gibbs free energy of formation for N$_2$ fixation over the (001) surface of ST and defected ST through alternating and distal mechanisms. The complete hydrogenation steps are considered for the most energetically favorable distal mechanism on the surface of DST.

standard reduction potential of nitrogen (N$_2$/NH$_3$). Similarly, for the oxidation of water, the VBM should lie below the standard oxidation potential of water (O$_2$/H$_2$O). Firstly, we have aligned the band edges of pristine with respect to the experimental observations and then the band edges of defected ST are aligned with respect to the pristine ST. The CBm of ST lies 0.8 V above the standard reduction potential of hydrogen (H$^+$/H$_2$).[61] The standard reduction potential of N$_2$ is 0.057 V above the standard reduction potential of hydrogen (Fig. 5d).[62] In pristine ST, the CBm is 0.74 V above the nitrogen reduction potential and the VBM is 1.18 V below the water oxidation potential, resulting in a total band gap of 3.21 eV. In defected ST, the defect states are above the nitrogen reduction potential and the band gap reduces to 2.86 eV (the gap between the lower defected state and the VBM). This is in line with the experimental observation of the band gap of 2.85 eV. The band edges are in accordance with the reduction of N$_2$ and the oxidation of H$_2$O. Thus, band edge alignment concludes that defected ST is more favorable for N$_2$ fixation.

Moreover, first-principles calculations are performed to calculate Gibbs free energy of formation (ΔG) for hydrogenation of adsorbed N$_2$ molecule on the surface of pristine and defected ST. The cleavage of the N≡N bond mainly determines the rate of reaction for N$_2$ fixation.[13] Therefore, the reaction rate is mainly determined by the free energy for *N$_2$H formation, which is usually the most energy-consuming step. Different possibilities of hydrogenation and adsorption lead to

different reaction pathways, namely distal and alternating. The adsorption of N$_2$ is more favorable on the TiO$_2$-plane surface than the SrO-plane surface since the transition element Ti efficiently promotes the cleavage of the N≡N bond by providing strong coordination. The N–N bond length of N$_2$ adsorbed on pristine and defected ST is 1.12 and 1.22 Å, respectively. The larger N–N bond length of N$_2$ adsorbed on defected ST is due to the more significant localized negative charge at the oxygen-vacancy site, making it more suitable for cleavage of the N–N bond. The cleavage of the N–N bond makes the N$_2$ molecule more favorable for further photocatalytic reaction. Fig. 5e shows the formation energies of the adsorbed N$_2$ molecules for sequential hydrogenation on surfaces of pristine and defected ST. The ΔG value is positive (+0.32 eV) for the first hydrogenation step of N$_2$ adsorbed on ST (001) surface with Ti-O$_2$ termination, hindering the initiation of nitrogen fixation. Calculations show that the Ti-O$_2$ surface with O-vacancy was a prominent active center that permitted stabilization of *N$_2$H. The ΔG value for the first step of hydrogenation of N$_2$ over a single O-vacancy is −0.35 eV, which is exothermic. The subsequent hydrogenation pathways are also energetically favorable, where the reaction mainly proceeds through the distal mechanism (see Fig. 5e). In addition, the N$_2$ adsorption was also favorable for ST with O-vacancy (ΔG = −0.41 eV) compared to pristine ST (ΔG = 0.66 eV) to initiate the activation process. Thus, O-vacancy creation considerably increases the catalytic activity of defected ST.

Besides, photoluminescence (PL) spectroscopy was performed to study the emission properties of as-synthesized materials. It has been reported that the emission intensity of PL spectra of semiconductor materials can be correlated with the extent of photogenerated charge recombination occurring in them.[63–65] The higher intensity of PL emission spectra signifies the more pronounced charge recombination in a particular material and *vice versa*. Herein, the PL spectra were collected at an excitation wavelength of 310 nm and the highest emission was observed at 387 nm for all the materials. It can be seen from Fig. S13† that pristine ST showed the strongest emission, which signifies the higher recombination of photogenerated charges in it. For DST1, the PL emission intensity was decreased in comparison to the pristine ST, which suggests lower recombination of photogenerated charges in it. For DST2, the PL emission intensity drastically decreased in comparison to the pristine ST with the indication of least charge recombination, but was slightly enhanced in the case of DST3. Thus, PL study infers the lowest recombination of photogenerated charges in DST2.

Based on these experimental and theoretical results, the superior photocatalytic N_2 fixation ability of DST2 can be ascribed to the appropriate amount of defects or surface active sites, enhanced surface area and suppressed recombination of photogenerated charges. A plausible mechanism has been proposed to explain the superior photocatalytic performance of DST2 material and depicted in Scheme 2a and b. The oxygen vacancies on the surface of DST materials serve as active sites for the chemisorption of N_2 molecules and activate them for the further photocatalytic process.[36,66] The electrons trapped in the oxygen vacancies get transferred to the lowest unoccupied molecular orbital of N_2 molecules, thereby resulting in a decreased bond order and hence their activation for further photocatalytic reduction. This activation of N_2 molecules enables the feasibility of photocatalytic NH_3 formation through proton-assisted N_2 reduction.[67] Furthermore, an experimental protocol has also been proposed based on the observations and results presented in this work (Scheme 2c). Definitely, the photocatalysts prepared by using nitrogen-based precursors contain surface nitrogenous contamination. Therefore, it is very important to examine the synthesized photocatalysts for surface nitrogenous impurities and eliminate them by using rigorous washing steps and their removal to the best extent should be
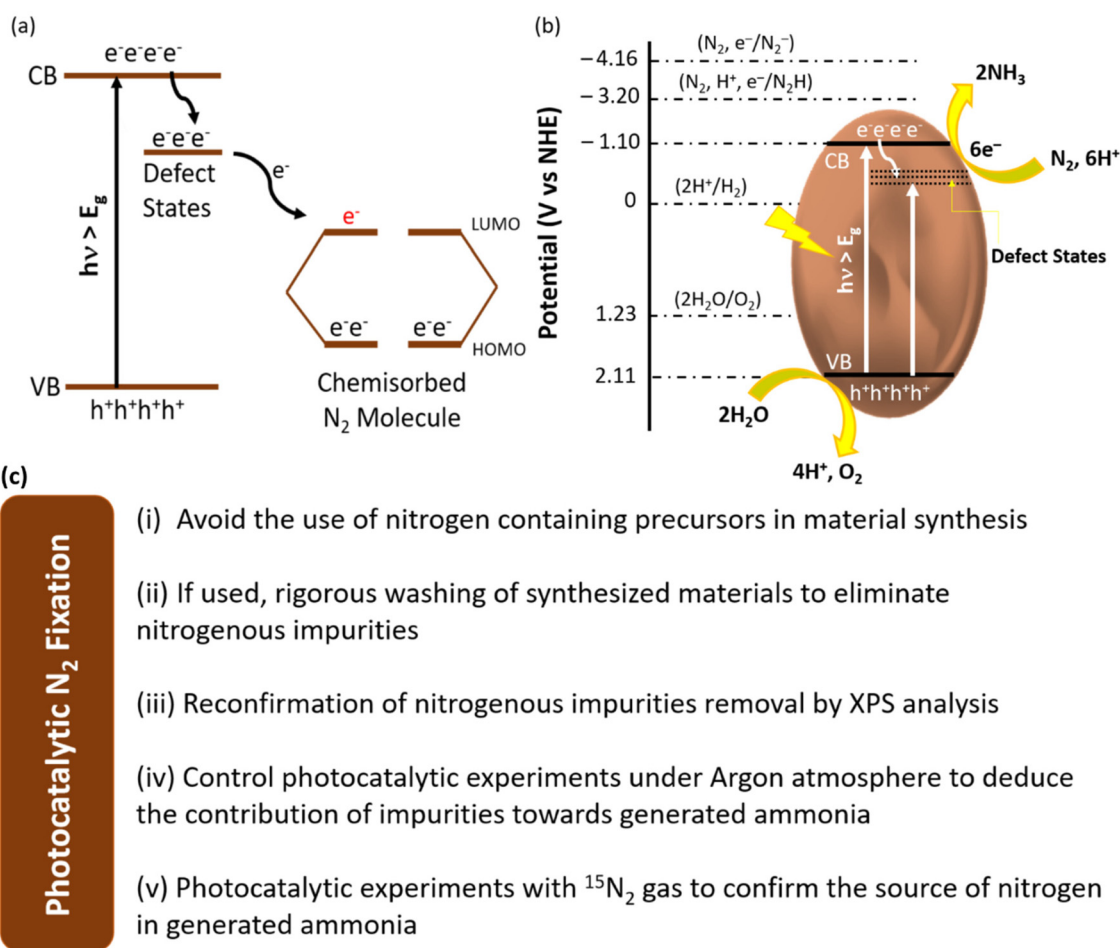
Scheme 2 Schematic illustration depicting the (a) activation of N_2 molecules by oxygen vacancies present on the surface of DST, (b) plausible mechanism of photocatalytic N_2 fixation over DST surface and (c) protocol for photocatalytic N_2 fixation experiments.

reconfirmed. The control photocatalytic experiments should be performed under Ar gas atmosphere to deduce the contribution of nitrogenous impurities towards photogenerated NH_3 and a realistic NH_3 production rate should be reported appropriately. Finally, the photocatalytic experiments with isotope-labeled $^{15}N_2$ gas should be performed to ensure the true photocatalytic activity of the synthesized materials.[2] Furthermore, it is suggested to avoid the use of nitrogen-based precursors in materials synthesis to eliminate the photocatalyst contamination problem in the beginning itself. Nevertheless, it is beneficial to investigate the surface of synthesized photocatalysts for nitrogenous contamination in each case so that realistic and reliable NH_3 production rates should be obtained and reported.[68]

4   Conclusion

In summary, $SrTiO_3$ nanocubes have been engineered with oxygen vacancies by using ascorbic acid as a reducing agent in a one-step solvothermal synthesis procedure. The XPS study revealed that the oxygen vacancies and Ti^{3+}-sites were formed over the $SrTiO_3$ surface when ascorbic acid was used as a reducing agent in the synthesis reaction. With an increase in the amount of ascorbic acid, the defects in the resulting DST catalysts were increased, which changed their appearance from pale to dark brown with a systematic decrease in the band gap. The well-defined nanocube morphology of pristine $SrTiO_3$ was also partially deformed with an increasing amount of ascorbic acid in the synthesis reaction as hollow cubes and porous aggregates were formed in the DST catalysts, which resulted in enhanced surface area. The photocatalytic performance of as-synthesized materials was examined by studying their N_2 fixation ability in pure water reaction conditions under natural sunlight irradiation. It was found that defect-engineered DST catalysts showed efficient N_2 fixation ability, whereas pristine $SrTiO_3$ was inactive for this reaction. The optimized DST2 catalyst showed the highest NH_3 formation with a rate of 14.41 μmol h^{-1}, which is ascribed to the efficient separation of photogenerated charges, enhanced specific surface area and an optimal amount of defects on its surface, which helps in the activation of N_2 molecules by their chemisorption and subsequent reduction by the photocatalytic action. Furthermore, the theoretical investigations infer that the N_2 fixation follows the distal pathway over the surface of defected ST. In addition, the importance of surface cleaning of photocatalysts and the deduction of contribution from impurities in NH_3 quantification are discussed in detail to provide a protocol for reporting realistic data in this field. The obtained results present the importance of defect engineering for the success of photocatalytic N_2 fixation reaction. It can be anticipated that this work can lead to the development of more efficient perovskite oxide based material in the near future by employing a similar strategy and direct the researchers to follow stringent experimental protocols to avoid the bogus reporting of NH_3 production rates.

Author contributions

Conflicts of interest

There are no conflicts to declare.

Acknowledgements

References

1   A. Kumar, A. Kumar and V. Krishnan, *ACS Catal.*, 2020, **10**, 10253–10315.
2   Y. Zhao, Y. Miao, C. Zhou and T. Zhang, *Mol. Catal.*, 2022, **518**, 112107.
3   K. Ithisuphalap, H. Zhang, L. Guo, Q. Yang, H. Yang and G. Wu, *Small Methods*, 2019, **3**, 1800352.
4   R. Lan, J. T. Irvine and S. Tao, *Int. J. Hydrogen Energy*, 2012, **37**, 1482–1494.
5   J. Lim, C. A. Fernández, S. W. Lee and M. C. Hatzell, *ACS Energy Lett.*, 2021, **6**, 3676–3685.
6   J. Wang, L. Guan, S. Yuan, J. Zhang, C. Zhao, X. Hu, B. Teng, Y. Wu and Y. He, *Sep. Purif. Technol.*, 2023, **314**, 123554.
7   A. Kumar and V. Krishnan, *Adv. Funct. Mater.*, 2021, **31**, 2009807.
8   R. Shi, X. Zhang, G. I. Waterhouse, Y. Zhao and T. Zhang, *Adv. Energy Mater.*, 2020, **10**, 2000659.
9   W. Zhang, J. Wang, X. Li, Y. Li, X. Hu, L. Zhao, Y. Wu and Y. He, *Green Energy Environ.*, 2023, **8**, 283–295.
10 J. Wang, C. Zhao, S. Yuan, X. Li, J. Zhang, X. Hu, H. Lin, Y. Wu and Y. He, *J. Colloid Interface Sci.*, 2023, **638**, 427–438.
11 A. Kumar, M. Kumar, V. Navakoteswara Rao, M. V. Shankar, S. Bhattacharya and V. Krishnan, *J. Mater. Chem. A*, 2021, **9**, 17006–17018.
12 R. Guan, D. Wang, Y. Zhang, C. Liu, W. Xu, J. Wang, Z. Zhao, M. Feng, Q. Shang and Z. Sun, *Appl. Catal., B*, 2021, **282**, 119580.

13 Y. Zhao, Y. Zhao, R. Shi, B. Wang, G. I. Waterhouse, L. Z. Wu, C. H. Tung and T. Zhang, *Adv. Mater.*, 2019, **31**, 1806482.

14 Z. He, Y. Wang, X. Dong, N. Zheng, H. Ma and X. Zhang, *RSC Adv.*, 2019, **9**, 21646–21652.

15 D. Wu, R. Wang, C. Yang, Y. An, H. Lu, H. Wang, K. Cao, Z. Gao, W. Zhang and F. Xu, *J. Colloid Interface Sci.*, 2019, **556**, 111–119.

16 X. Xue, R. Chen, H. Chen, Y. Hu, Q. Ding, Z. Liu, L. Ma, G. Zhu, W. Zhang and Q. Yu, *Nano Lett.*, 2018, **18**, 7372–7377.

17 Y. Bi, Y. Wang, X. Dong, N. Zheng, H. Ma and X. Zhang, *RSC Adv.*, 2018, **8**, 21871–21878.

18 P. Li, Z. Zhou, Q. Wang, M. Guo, S. Chen, J. Low, R. Long, W. Liu, P. Ding and Y. Wu, *J. Am. Chem. Soc.*, 2020, **142**, 12430–12439.

19 Y. Zhang, J. Di, P. Ding, J. Zhao, K. Gu, X. Chen, C. Yan, S. Yin, J. Xia and H. Li, *J. Colloid Interface Sci.*, 2019, **553**, 530–539.

20 Y. Shiraishi, S. Shiota, Y. Kofuji, M. Hashimoto, K. Chishiro, H. Hirakawa, S. Tanaka, S. Ichikawa and T. Hirai, *ACS Appl. Energy Mater.*, 2018, **1**, 4169–4177.

21 A. Kumar, V. Navakoteswara Rao, A. Kumar, M. Venkatakrishnan Shankar and V. Krishnan, *ChemPhotoChem*, 2020, **4**, 427–444.

22 A. Kumar, S. Kumar, A. Bahuguna, A. Kumar, V. Sharma and V. Krishnan, *Mater. Chem. Front.*, 2017, **1**, 2391–2404.

23 A. Kumar, S. Kumar and V. Krishnan, *Nanophotocatalysis and Environmental Applications: Materials and Technology*, 2019, pp. 139–165.

24 A. Kumar, V. Navakoteswara Rao, A. Kumar, A. Mushtaq, L. Sharma, A. Halder, S. K. Pal, M. V. Shankar and V. Krishnan, *ACS Appl. Energy Mater.*, 2020, **3**, 12134–12147.

25 S. Patial, V. Hasija, P. Raizada, P. Singh, A. A. P. K. Singh and A. M. Asiri, *J. Environ. Chem. Eng.*, 2020, **8**, 103791.

26 M. Sharma, A. Kumar and V. Krishnan, *Nanotechnology*, 2022, **33**, 275702.

27 J. Pi, X. Jia, Z. Long, S. Yang, H. Wu, D. Zhou, Q. Wang, H. Zheng, Y. Yang, J. Zhang and J. Qiu, *Adv. Energy Mater.*, 2022, **12**, 2202074.

28 H. Tan, Z. Zhao, W.-b. Zhu, E. N. Coker, B. Li, M. Zheng, W. Yu, H. Fan and Z. Sun, *ACS Appl. Mater. Interfaces*, 2014, **6**, 19184–19190.

29 T. Yu, Z. Lv, K. Wang, K. Sun, X. Liu, G. Wang, L. Jiang and G. Xie, *J. Power Sources*, 2019, **438**, 227014.

30 X. Zhou, N. Liu, T. Yokosawa, A. Osvet, M. E. Miehlich, K. Meyer, E. Spiecker and P. Schmuki, *ACS Appl. Mater. Interfaces*, 2018, **10**, 29532–29542.

31 G. Zhang, W. Jiang, S. Hua, H. Zhao, L. Zhang and Z. Sun, *Nanoscale*, 2016, **8**, 16963–16968.

32 B. Huang, Y. Liu, Q. Pang, X. Zhang, H. Wang and P. K. Shen, *J. Mater. Chem. A*, 2020, **8**, 22251–22256.

33 J. Wang, T. Wang, Z. Zhao, R. Wang, C. Wang, F. Zhou, S. Li, L. Zhao and M. Feng, *J. Alloys Compd.*, 2022, **902**, 163865.

34 K. Ariga, *Nanoscale Horiz.*, 2021, **6**, 364–378.

35 Q. Zhang, Y. Huang, L. Xu, J.-j. Cao, W. Ho and S. C. Lee, *ACS Appl. Mater. Interfaces*, 2016, **8**, 4165–4174.

36 H. Li, J. Shang, Z. Ai and L. Zhang, *J. Am. Chem. Soc.*, 2015, **137**, 6393–6399.

37 Z.-K. Shen, Y.-J. Yuan, P. Wang, W. Bai, L. Pei, S. Wu, Z.-T. Yu and Z. Zou, *ACS Appl. Mater. Interfaces*, 2020, **12**, 17343–17352.

38 G. Zhang, X. Yang, C. He, P. Zhang and H. Mi, *J. Mater. Chem. A*, 2020, **8**, 334–341.

39 X. Zhao, X. Lan, D. Yu, H. Fu, Z. Liu and T. Mu, *Chem. Commun.*, 2018, **54**, 13010–13013.

40 D. Zhu, L. Zhang, R. E. Ruther and R. J. Hamers, *Nat. Mater.*, 2013, **12**, 836–841.

41 W. Zhao, W. Zhao, G. Zhu, T. Lin, F. Xu and F. Huang, *CrystEngComm*, 2015, **17**, 7528–7534.

42 Z. Zheng, B. Huang, J. Lu, Z. Wang, X. Qin, X. Zhang, Y. Dai and M.-H. Whangbo, *Chem. Commun.*, 2012, **48**, 5733–5735.

43 Z. Wang, C. Yang, T. Lin, H. Yin, P. Chen, D. Wan, F. Xu, F. Huang, J. Lin and X. Xie, *Energy Environ. Sci.*, 2013, **6**, 3007–3014.

44 Y. Xiao, S. Chen, Y. Wang, Z. Hu, H. Zhao and W. Xie, *Nanomaterials*, 2019, **9**, 883.

45 H. Liu, H. Ma, X. Li, W. Li, M. Wu and X. Bao, *Chemosphere*, 2003, **50**, 39–46.

46 X. Pan, M.-Q. Yang, X. Fu, N. Zhang and Y.-J. Xu, *Nanoscale*, 2013, **5**, 3601–3614.

47 L. Hao, K. Miyazawa, H. Yoshida and Y. Lu, *Mater. Res. Bull.*, 2018, **97**, 13–18.

48 L.-L. Feng, X. Zou, J. Zhao, L.-J. Zhou, D.-J. Wang, X. Zhang and G.-D. Li, *Chem. Commun.*, 2013, **49**, 9788–9790.

49 H. Tan, Z. Zhao, M. Niu, C. Mao, D. Cao, D. Cheng, P. Feng and Z. Sun, *Nanoscale*, 2014, **6**, 10216–10223.

50 Y. Bourlier, M. Bouttemy, O. Patard, P. Gamarra, S. Piotrowicz, J. Vigneron, R. Aubry, S. Delage and A. Etcheberry, *ECS J. Solid State Sci. Technol.*, 2018, **7**, P329.

51 Y. Xia, Z. He, Y. Lu, B. Tang, S. Sun, J. Su and X. Li, *RSC Adv.*, 2018, **8**, 5441–5450.

52 G. Xing, L. Zhao, T. Sun, Y. Su and X. Wang, *SpringerPlus*, 2016, **5**, 1–13.

53 Y. Su, S. Huang, T. Wang, L. Peng and X. Wang, *J. Hazard. Mater.*, 2015, **295**, 119–126.

54 A. Naldoni, M. Allieta, S. Santangelo, M. Marelli, F. Fabbri, S. Cappelli, C. L. Bianchi, R. Psaro and V. Dal Santo, *J. Am. Chem. Soc.*, 2012, **134**, 7600–7603.

55 S. Cho, H. Jeong, D.-H. Park, S.-H. Jung, H.-J. Kim and K.-H. Lee, *CrystEngComm*, 2010, **12**, 968–976.

56 A. Ortega, M. Gómez, J. L. Domingo and J. Corbella, *Arch. Environ. Contam. Toxicol.*, 1989, **18**, 612–616.

57 P. Makuła, M. Pacia and W. Macyk, *J. Phys. Chem. Lett.*, 2018, **9**, 6814–6817.

58 Z. Ying, S. Chen, T. Peng, R. Li and J. Zhang, *Eur. J. Inorg. Chem.*, 2019, **2019**, 2182–2192.

59 H. Li, C. Mao, H. Shang, Z. Yang, Z. Ai and L. Zhang, *Nanoscale*, 2018, **10**, 15429–15435.

60 Y. Zhao, R. Shi, X. Bian, C. Zhou, Y. Zhao, S. Zhang, F. Wu, G. I. Waterhouse, L. Z. Wu and C. H. Tung, *Adv. Sci.*, 2019, **6**, 1802109.

61 M. Kumar, P. Basera, S. Saini and S. Bhattacharya, *J. Phys. Chem. C*, 2020, **124**, 10272–10279.

62 W. Guo, K. Zhang, Z. Liang, R. Zou and Q. Xu, *Chem. Soc. Rev.*, 2019, **48**, 5658–5716.

63 A. Kumar, C. Schuerings, S. Kumar, A. Kumar and V. Krishnan, *Beilstein J. Nanotechnol.*, 2018, **9**, 671–685.

64 Y. Yan, H. Yang, X. Zhao, R. Li and X. Wang, *Mater. Res. Bull.*, 2018, **105**, 286–290.

65 A. Kumar, Y. Singla, M. Sharma, A. Bhardwaj and V. Krishnan, *Chemosphere*, 2022, **308**, 136212.

66 H. Hirakawa, M. Hashimoto, Y. Shiraishi and T. Hirai, *J. Am. Chem. Soc.*, 2017, **139**, 10929–10936.

67 Y. Huang, N. Zhang, Z. Wu and X. Xie, *J. Mater. Chem. A*, 2020, **8**, 4978–4995.

68 P.-W. Huang and M. C. Hatzell, *Nat. Commun.*, 2022, **13**, 7908.